electronics

Article

A Hybrid Inductive Power Transfer System with High Misalignment Tolerance Using Double-DD Quadrature Pads

Zhaowei Gong [1,2,*], Jingang Li [1], Xiangqian Tong [1] and Yongsheng Fu [2]

[1] School of Electrical Engineering, Xi'an University of Technology, 58, Yanxiang Rd., Xi'an 710054, China; lijingang@xaut.edu.cn (J.L.); xqtong@xaut.edu.cn (X.T.)
[2] School of Electronic Information Engineering, Xi'an Technological University, 2, Xuefu Rd., Xi'an 710021, China; fys060409@126.com
* Correspondence: gongzhaowei@xatu.edu.cn

Abstract: Inductive power transfer (IPT) has been widely adopted as an efficient and convenient charging manner for both static and in-motion EVs. In this paper, a new hybrid topology is presented to improve the coupling tolerance under pad misalignment. The double inductor–capacitor–capacitor (LCC-LCC) network and series hybrid network combining the LCC-LCC topology and series-series (SS) topology are connected in parallel to provide better tolerance against self- and mutual inductance changes, particularly with a large *Z*-axis transmission distance. A double-DD quadrature pad (DD2Q) consists of a Q pad, and double orthogonal DD pads are analyzed in detail, which are employed to decouple the cross-mutual inductance. Moreover, a parametric design method based on the misalignment characteristics of the DD2Q pads is also proposed to maintain relatively constant power output. A 650-W hybrid topology with a fixed operating frequency of 85 kHz was built to verify the system's feasibility. The size of the DD2Q pads was 280 mm × 280 mm, and the air gap was 100 mm. The results clearly show that the proposed hybrid topology can achieve a fluctuation within 5% in the output current with load varying from 100% full load to 25% light load conditions when the *Z*-axis transmission distance varies from 80 mm to 150 mm, and the maximum efficiency can reach 91% when the *Z*-axis transmission distance is 80 mm.

Keywords: inductive power transfer; DD2Q pads; hybrid topology; misalignment tolerance

check for updates

Citation: Gong, Z.; Li, J.; Tong, X.; Fu, Y. A Hybrid Inductive Power Transfer System with High Misalignment Tolerance Using Double-DD Quadrature Pads. *Electronics* **2022**, *11*, 2228. https://doi.org/10.3390/electronics11142228

Academic Editors: Fengwei Chen, Hongsheng Hu, Lei Zhao, Hao Feng and Xiaoming Zhang

Received: 22 June 2022
Accepted: 15 July 2022
Published: 17 July 2022

1. Introduction

An IPT system can deliver power over relatively large air gaps via magnetic couplings, including a high-frequency inverter, compensation topology, coupling coils, and charging circuits. An IPT system has the excellent advantages of safety with galvanic isolation [1], high reliability [2], and being environmentally friendly [3] compared with traditional conductive charging technology. Nowadays, the IPT system has been widely employed in powering electronic applications, such as low-power portable electronic devices, implantable medical instruments [4], electric vehicle (EV) charging [5], and autonomous underwater power supplies [6]. Much research has been conducted by numerous organizations, such as the Massachusetts Institute of Technology (MIT), Auckland University, Korea Advanced Institute of Science and Technology (KAIST), and Oak Ridge National Laboratory (ORNL).

The misalignments between the primary and secondary magnetic couplers can cause the variation of self-inductances and mutual inductances, which may in practice lead to a reduction in power transfer, instability of the system, and increased power losses. Aside from that, the equivalent load varies during the battery charging process [7]. Therefore, the goal of this paper is to design an IPT system with high misalignment tolerance and load-independent current output.

In order to improve the misalignment tolerance of the IPT system, some control schemes, such as increasing DC-DC conversion [8,9], phase shift control, and variable frequency control [10–15], have been proposed to modulate the output current or voltage. The additional DC-DC converter combines with MOSFET, the filter inductor and capacitor, and the driver circuit, which results in extra volume and cost and decreasing the system efficiency. The phase shift control and variable frequency control usually need a wireless communication device to collect the voltage and current signals of the secondary side to realize closed-loop control. However, wireless communications can be interrupted in highly magnetic conditions, which may result in instability of the IPT system. Moreover, phase shift control may not achieve ZVS under a wide range of loads, which increases the switching loss, and variable frequency control may result in bifurcation phenomena and decreasing the output power. Hence, in order to solve the above-mentioned defects, considerable efforts focus on proper magnetic coupler design [16–21], such as bipolar and double-D pads, tripolar pads, quadruple-D pads, and unsymmetrical pads, which can offer a relatively uniform magnetic distribution. For example, the quadruple-D pads are proposed in [16] to be tolerant to lateral misalignment, which consists double quadrature coils at the primary and secondary sides. Tripolar pads are proposed in [18] to improve the omnidirectional misalignment tolerance. However, these tripolar pads need to consist of three inverters at the primary side. That aside, unsymmetrical pads are presented in [19] to minimize the cost of copper and the size of the coil structure, adopting the method of concentrated magnetic flux to achieve misalignment tolerance. As an alternative method, hybrid topologies combining two different topologies with opposite output trends are implemented to maintain a stable output under misalignment conditions. A hybrid topology combines with LCC-LCC and SS topologies [20,21] to realize relatively constant power output within 50% Y-axis misalignment. In [22], LCC-S and S-LCC topologies are employed to tolerate 50% X-axis pad misalignment, where the primary sides are connected in parallel and the secondary sides are connected in series. Although the previous hybrid topologies are able to tolerate a pad's special misalignment, as shown in Figure 1, the working range of misalignment tolerance is still narrow. Therefore, better misalignment tolerance, particularly with Z-axis tolerance for different EV class heights with a wider coupling variation range, is desired, which is identified as the research gap for this research.

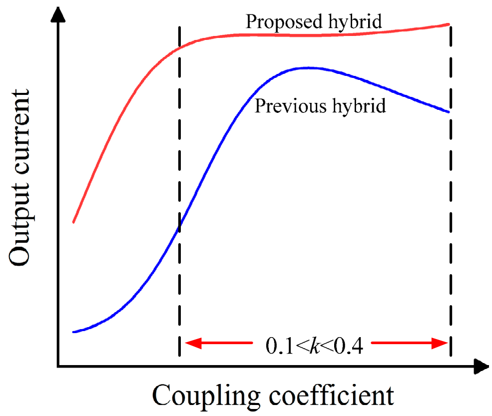

Figure 1. Comparison of the different topologies.

This paper presents a new hybrid topology using DD2Q pads to achieve stable output power at a large vertical misalignment, and the main contributions of this article are summarized as follows:

(1) This article proposes a new hybrid IPT system with high misalignment tolerance. The hybrid system consists of a series hybrid topology and LCC-LCC topology. The series hybrid topology and LCC-LCC topology are connected in parallel at the primary side and secondary side. The proposed approach can improve the output power compared with the single compensation topology and reduce the switch voltage stress. Moreover, the proposed hybrid IPT system can achieve a near load-independent current output.

(2) DD2Q pads are used in the hybrid IPT system, which consist of a single-Q coil and double-DD coils. The size of the DD2Q pads is 280 mm × 280 mm, and the air gap is 100 mm. The double-DD coils are orthogonally placed, and the Q coil is placed in a centrally symmetric position, which can realize decoupling of the DD and Q coils on the same side of the primary and secondary sides. Therefore, the independent current output of the series hybrid topology and LCC-LCC topology can be achieved.

(3) A parameter optimization method based on DD2Q mutual inductances is proposed to realize a relatively constant output current with high misalignment tolerance, which is able to simplify the control complexity. By using the monotonic decreasing characteristic of the series hybrid topology and monotonic increasing characteristic of the LCC-LCC topology to realize the complementary output of the two topologies, the output current is ensured to be relatively stable.

Specifically, the mathematical model of the proposed hybrid topology is systematically analyzed in Section 2. In Section 3, the mutual inductance characteristics of the DD2Q pads and the parameter optimization are presented. The experimental results are provided in Section 4 to verify the theoretical analysis. Finally, the conclusion is drawn in Section 5.

2. Theoretical Analysis

The circuit of the proposed hybrid IPT system is shown in Figure 2, which consists of a series hybrid topology and LCC-LCC topology. The high-frequency inverter combines with four MOSFETs (Q_1–Q_4). Inductor L_0 and capacitors C_0, C_1, and C_3 (L_7, C_2, C_4, and C_7) constitute the series hybrid topology, while inductor L_8 and capacitors C_5 and C_8 (L_9, C_6, and C_9) constitute the LCC-LCC compensation topology. The primary and secondary sides of the series hybrid topology and LCC-LCC topology are both connected in parallel, together forming the proposed hybrid topology. The main magnetic coupling between the coils is M_{12}, M_{34}, and M_{56}. The full-bridge rectifier comprises four diodes (D_1–D_4). Because the inductor $L_0(L_7)$ and capacitor $C_3(C_4)$ are connected in series in the proposed hybrid topology, and therefore they can be treated as a passive component, such as inductor L_e or capacitor C_e, which can be expressed as [16]

$$\begin{cases} j\omega L_e = j\omega L_0 + 1/j\omega C_3, \text{ if } \omega L_0 - 1/\omega C_3 > 0 \\ 1/j\omega C_e = j\omega L_0 + 1/j\omega C_3 \text{ if } \omega L_0 - 1/\omega C_3 < 0 \end{cases} \tag{1}$$

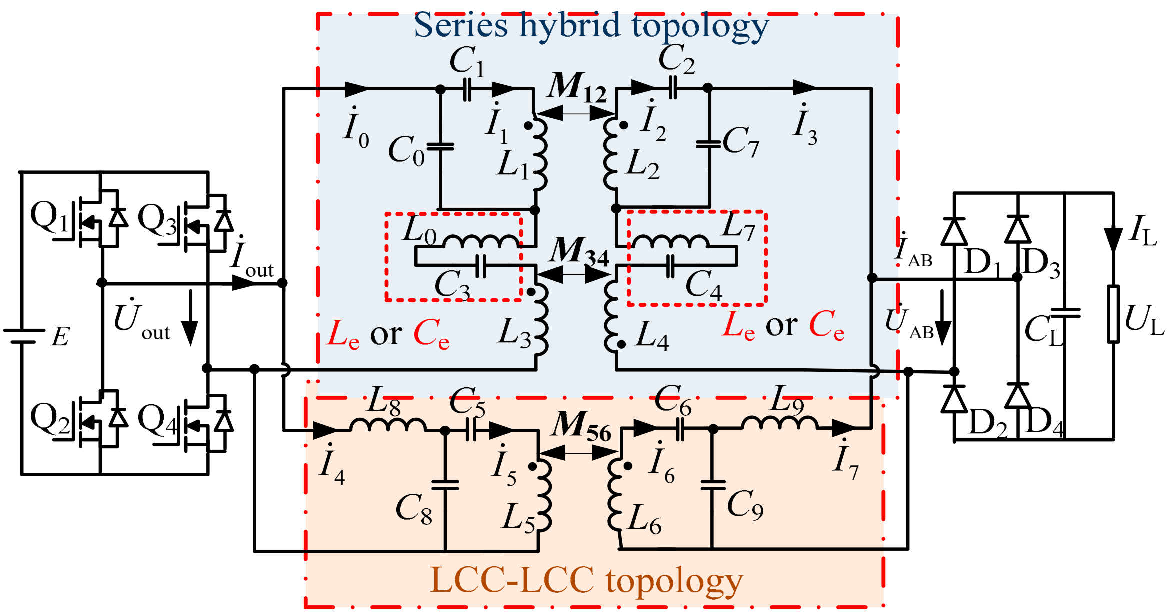

Figure 2. Proposed hybrid IPT system.

The full-bridge rectifier is adopted in the secondary side, and thus the input voltage U_{AB}, the input current I_{AB}, and the equivalent resistance R_{AB} of the rectifier can be expressed as [8].

$$\begin{cases} U_{\mathrm{AB}} = \frac{2\sqrt{2}}{\pi} U_{\mathrm{L}} \\ I_{\mathrm{AB}} = \frac{\pi\sqrt{2}}{4} I_{\mathrm{L}} \\ R_{\mathrm{AB}} = \frac{8}{\pi^2} R_{\mathrm{L}} \end{cases} \tag{2}$$

2.1. Analysis of the Series Hybrid Topology

The circuit of the series hybrid topology is shown in Figure 3, where U_{out} is a high-frequency inverter output voltage. In order to minimize the VA rating of the power inverter, the compensation networks are tuned to the same resonant angular frequency ω. Thus, the resonant parameters should satisfy the following equations:

$$\begin{cases} \omega^2 L_0 C_0 = \omega^2 L_1 \frac{C_0 C_1}{C_0 + C_1} = 1 \\ \omega^2 L_7 C_7 = \omega^2 L_2 \frac{C_2 C_7}{C_2 + C_7} = 1 \\ \omega^2 L_3 C_3 = \omega^2 L_4 C_4 = 1 \end{cases} . \tag{3}$$

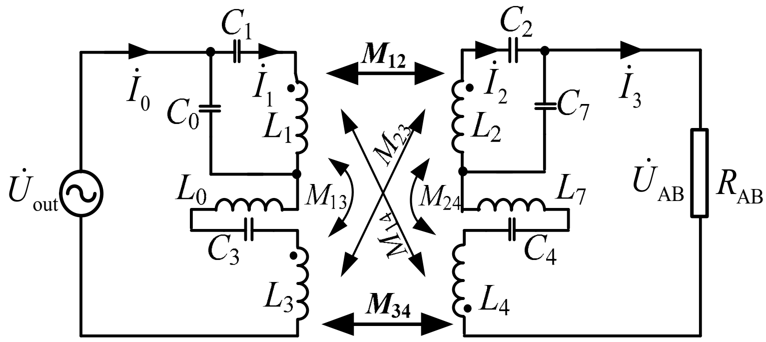

Figure 3. The series hybrid topology driven by a voltage source.

According to Kirchhoff's voltage law, we can find

$$\begin{bmatrix} Z_{00} & Z_{01} & Z_{02} & Z_{03} \\ Z_{10} & Z_{11} & Z_{12} & Z_{13} \\ Z_{20} & Z_{21} & Z_{22} & Z_{23} \\ Z_{30} & Z_{31} & Z_{32} & Z_{33} \end{bmatrix} \begin{bmatrix} \dot{I}_0 \\ \dot{I}_1 \\ \dot{I}_2 \\ \dot{I}_3 \end{bmatrix} = \begin{bmatrix} \dot{U}_{\mathrm{out}} \\ 0 \\ 0 \\ 0 \end{bmatrix} \tag{4}$$

where $Z_{20} = j\omega M_{23} Z_{00} = j\omega L_0 + (j\omega C_0)^{-1} + j\omega L_3 + (j\omega C_3)^{-1}$, $Z_{01} = -(j\omega C_0)^{-1} + j\omega M_{13}$, $Z_{02} = -j\omega M_{23}$, $Z_{03} = j\omega M_{34}$, $Z_{10} = j\omega M_{13} - (j\omega C_0)^{-1}$, $Z_{11} = j\omega L_1 + (j\omega C_0)^{-1} + (j\omega C_1)^{-1}$, $Z_{12} = -j\omega M_{12}$, $Z_{13} = j\omega M_{14}$, $Z_{21} = j\omega M_{12}$, $Z_{22} = j\omega L_2 + (j\omega C_2)^{-1} + (j\omega C_7)^{-1}$, $Z_{23} = (j\omega C_7)^{-1} + j\omega M_{24}$, $Z_{30} = j\omega M_{34}$, $Z_{31} = j\omega M_{14}$, $Z_{32} = -(j\omega C_7)^{-1} - j\omega M_{24}$, $Z_{33} = j\omega L_7 + (j\omega C_7)^{-1} + j\omega L_4 + (j\omega C_4)^{-1} + R_{\mathrm{AB}}$.

By designing proper coupling structures, which will be discussed in Section 3, the effects of the cross couplings (M_{13}, M_{14}, M_{23}, and M_{24}) on the output can be ignored. Hence, by solving Equation (4), the currents are expressed by

$$\begin{cases} \dot{I}_0 = \frac{\dot{U}_{\mathrm{out}}}{\omega^2} \frac{M_{12}^2 R_{\mathrm{AB}}}{(L_0 L_7 + M_{12} M_{34})^2} \\ \dot{I}_3 = \frac{\dot{U}_{\mathrm{out}}}{j\omega} \frac{M_{12}}{L_0 L_7 + M_{12} M_{34}} \end{cases} \tag{5}$$

According to Equation (5), the input equivalent impedance $Z_{\text{in-series}}$ of the series hybrid system can be deduced to be

$$Z_{\text{in-series}} = \frac{\omega^2 (L_0 L_7 + M_{12} M_{34})^2}{M_{12}{}^2 R_{\text{AB}}} \tag{6}$$

According to Equations (5) and (6), the series hybrid topology can achieve zero phase angle (ZPA). Aside from that, the output current I_3 is related to the inverter output voltage U_{out}, resonant angular frequency ω, inductors L_0 and L_7, and mutual inductances M_{12} and M_{34}. In order to achieve symmetry between the primary and secondary circuits, inductors L_0 and L_7 are usually assumed to be the same. The main mutual inductances M_{12} and M_{34} are assumed to have the linear trend with the air gap, which will be discussed in Section 3. Therefore, the output current of the series hybrid topology is shown in Figure 4, where all the related parameter values will be listed in Table 1. It is obvious that the output current I_3 shows a downward concave parabolic trend with the decrease in the mutual inductance. Although the series hybrid topology has a certain misalignment tolerance, the operating range is still narrow.

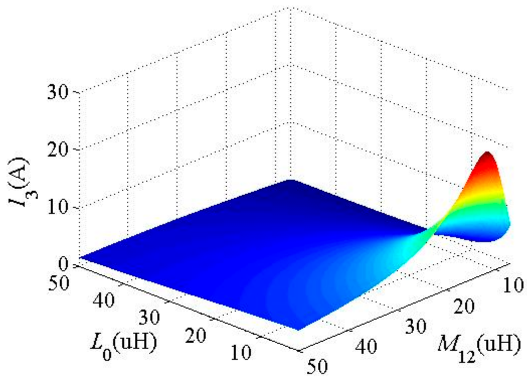

Figure 4. Output current of the series hybrid topology.

Table 1. Parameter values of the experimental platform.

Parameter	Value	Parameter	Value
f	85 kHz	C_0	232.2 nF
L_1	15.1 uH	C_1	25.8 nF
L_2	150.1 uH	C_2	25.7 nF
L_3	149.8 uH	C_5	27.8 nF
L_4	156.1 uH	C_6	27.7 nF
L_5	156.0 uH	C_7	232.2 nF
L_6	160.1 uH	C_8	110.2 nF
L_8	32.2 uH	C_9	110.3 nF
L_9	32.1 uH	E	70 V
C_e	25.1 nF		

2.2. Analysis of the LCC-LCC Topology

Figure 5 shows the LCC-LCC equivalent circuit, where U_{out} is also a high-frequency inverter output voltage. The compensation topology is tuned to the same resonant angular frequency ω. Therefore, the resonant tanks should satisfy the following equations:

$$\begin{cases} \omega^2 L_8 C_8 = \omega^2 L_5 \frac{C_5 C_8}{C_5 + C_8} = 1 \\ \omega^2 L_9 C_9 = \omega^2 L_6 \frac{C_6 C_9}{C_6 + C_9} = 1 \end{cases} \tag{7}$$

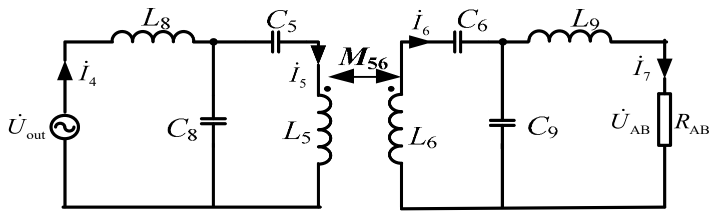

Figure 5. LCC-LCC topology circuit.

According to Kirchhoff's voltage law, we find

$$\begin{bmatrix} Z_{00} & Z_{01} & 0 & 0 \\ Z_{10} & Z_{11} & Z_{12} & 0 \\ 0 & Z_{21} & Z_{22} & Z_{23} \\ 0 & 0 & Z_{32} & Z_{33} \end{bmatrix} \begin{bmatrix} \dot{I}_4 \\ \dot{I}_5 \\ \dot{I}_6 \\ \dot{I}_7 \end{bmatrix} = \begin{bmatrix} \dot{U}_{\text{out}} \\ 0 \\ 0 \\ 0 \end{bmatrix} \tag{8}$$

where $Z_{00} = j\omega L_8 + (j\omega C_8)^{-1}$, $Z_{01} = Z_{10} = -(j\omega C_8)^{-1}$, $Z_{11} = (j\omega C_8)^{-1} + (j\omega C_5)^{-1} + j\omega L_5$, $Z_{12} = Z_{21} = -j\omega M_{56}$, $Z_{22} = j\omega L_6 + (j\omega C_6)^{-1} + (j\omega C_9)^{-1}$, $Z_{23} = Z_{32} = -(j\omega C_9)^{-1}$, $Z_{33} = j\omega L_9 + (j\omega C_9)^{-1} + R_{\text{AB}}$.

By solving Equation (8), the currents are yielded as

$$\begin{cases} \dot{I}_4 = \frac{M_{56}^2 \dot{U}_{\text{out}} R_{\text{AB}}}{\omega^2 L_8^2 L_9^2} \\ \dot{I}_7 = \frac{M_{56} \dot{U}_{\text{out}}}{j\omega L_8 L_9} \end{cases} \tag{9}$$

According to Equation (9), the output voltage of the inverter is also in the same phase with the current, which aids in maintaining ZVS across the entire operating region and improving the output efficiency of the system. The output current I_7 is related to the inverter output voltage U_{out}, resonant angular frequency ω, inductors L_8 and L_9, and mutual inductance M_{56}. In this paper, inductors L_8 and L_9 are also assumed to be the same. Therefore, the output current I_7 is shown in Figure 6, where all the related parameter values will be listed in Table 1. It is clear that the output current I_7 shows a monotonous downward trend with the decrease in the mutual inductance.

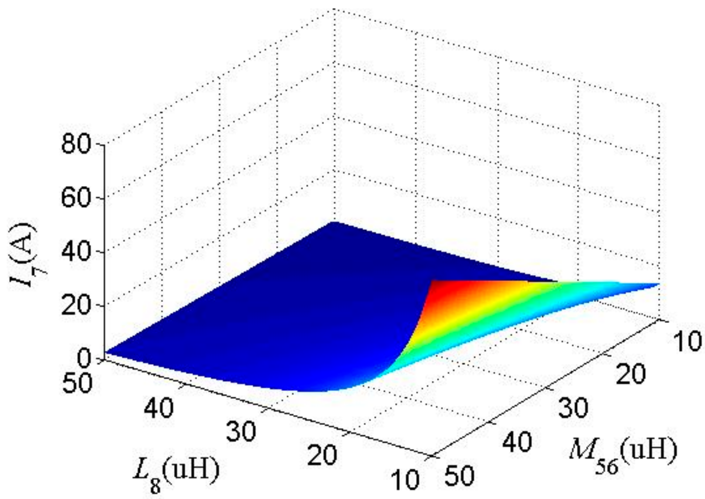

Figure 6. Output current of the LCC-LCC topology.

Therefore, the series hybrid compensation network and the LCC-LCC compensation network can be connected in parallel at the transmitter and the receiver, which is conductive to achieving a relatively constant power output with large misalignment.

2.3. Analysis of the Proposed Hybrid Topology

According to Equations (5) and (9), the total output current of the inverter is expressed by

$$\dot{I}_{\text{out}} = \dot{I}_0 + \dot{I}_4 = \frac{\dot{U}_{\text{out}} R_{\text{AB}}}{\omega^2} \left(\frac{M_{12}^2}{(L_0 L_7 + M_{12} M_{34})^2} + \frac{M_{56}^2}{(L_8 L_9)^2} \right) \tag{10}$$

Then, the total input equivalent impedance of the proposed hybrid topology can be given by

$$Z_{\text{in}} = \frac{\dot{U}_{\text{out}}}{\dot{I}_{\text{out}}} = \frac{\omega^2}{R_{\text{AB}}} \frac{1}{\frac{M_{12}^2}{(L_0 L_7 + M_{12} M_{34})^2} + \frac{M_{56}^2}{(L_8 L_9)^2}} \tag{11}$$

From Equations (10) and (11), the total input impedance of the proposed hybrid topology is purely resistant, which aids to improving the overall transmission efficiency.

According to the characteristics of the parallel circuit, the total output current of the proposed hybrid topology can be expressed as

$$\dot{I}_{\text{AB}} = \dot{I}_3 + \dot{I}_7 = \frac{\dot{U}_{\text{out}}}{j\omega} \left(\frac{M_{12}}{L_0 L_7 + M_{12} M_{34}} + \frac{M_{56}}{L_8 L_9} \right) \tag{12}$$

From Equation (12), the system can realize a load-independent current output. When misalignment occurs, the main mutual inductance M_{12}, M_{34}, and M_{56} will drop at the same time. By designing appropriate compensating inductors L_0, L_7, L_8, and L_9, the constant current output can be realized in a certain range of misalignment.

3. Parametric Design of the Proposed Hybrid Topology

3.1. Misalignment Analysis of DD2Q Pads

As analyzed in Section 2, the expected coupling pad should have the following characteristics:

(1) The expected coupling pad should consist of three transmitters and three receivers.
(2) The cross mutual inductances are designed to be zero or small enough when misalignment occurs, and thus the proposed hybrid topology can realize a load-independent output.

Recently, the DDQ and DD coils have had anti-misalignment characteristics, which can realize decoupling in the *X*- and *Z*-axis to eliminate the influence of cross-coupling. However, these two coupling coil structures can only be applied to four-coil structures. Based on the DD coil and DDQ coil, the DD2Q coil structure is proposed in this paper, as shown in Figure 7. The DD2Q coils consist of a single-Q coil and double-DD coils, and there are three coils at both the transmitter and receiver sides. The size of the Q coil is 280 mm × 280 mm, the size of the DD coil is 280 mm × 280 mm, and the *Z*-axis transmission distance is 100 mm.

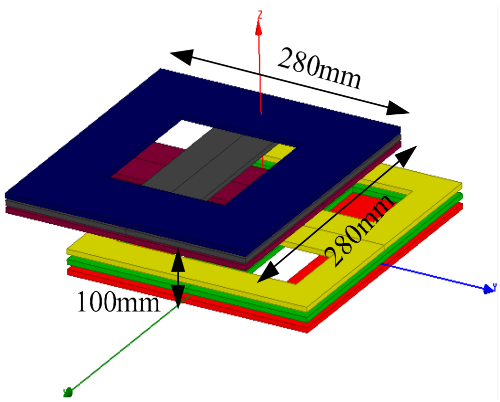

Figure 7. Structure of the proposed DD2Q pads.

The misalignment between the primary and pick-up pads is unavoidable in the charging system, including the *X*-axis, *Y*-axis, *Z*-axis, and *XY*-axis. Therefore, Figure 8 shows the measured mutual inductances of the DD2Q pads with misalignment along the *X*-, *Y*-, *Z*-, and *XY*-axes separately.

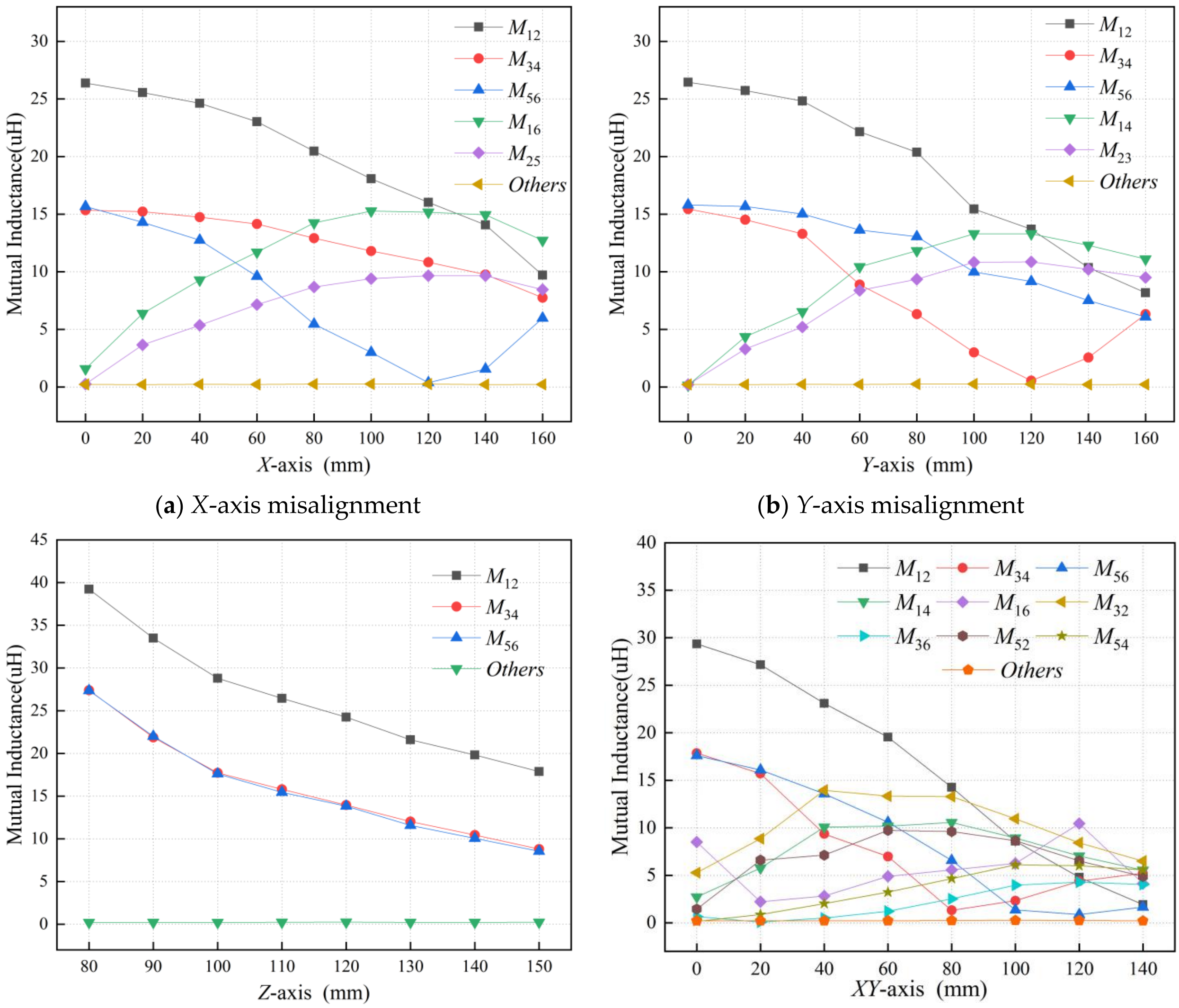

(**a**) *X*-axis misalignment (**b**) *Y*-axis misalignment

(**c**) *Z*-axis misalignment (**d**) *XY*-axis diagonal misalignment

Figure 8. Measured mutual inductances of DD2Q coils.

Obviously, the main mutual inductances M_{12}, M_{34}, and M_{56} and the cross-coupling mutual inductances vary significantly when *X*-axis, *Y*-axis, and *XY*-axis diagonal misalignments occur in Figure 8a,b,d. The reason for this is that non-orthogonal magnetic flux is coupled in the *X*-axis, *Y*-axis and *XY*-axis diagonal misalignments. The main mutual inductances M_{12}, M_{34}, and M_{56} show a linear decreasing trend with the *Z*-axis transmission distance, and the cross-couplings are too small to be ignored, as shown in Figure 8c. Moreover, the main mutual inductances (M_{34} and M_{56}) of the double orthogonal DD pads have the same change trend at the *Z*-axis transmission distance. Therefore, the proposed hybrid topology cannot provide a constant current output in the *X*-axis and *Y*-axis misalignments, as analyzed in Section 2. In many applications, such as cars, SUVs, and trucks, the *X*-axis and *Y*-axis misalignments can be adjusted by auxiliary devices for cars, such as a reversing camera and reversing radar, but the vertical air gap is hard to adjust. Hence, the DD2Q coils are fit for the proposed hybrid topology with a relatively constant current output, where the vertical direction changes dramatically.

3.2. Parametric Design Method

The design of compensation parameters is of great importance to realize a relatively constant output within the maximal misalignment. A parametric design method based on inductances L_0, L_7, L_8, and L_9 is presented to maintain the output current in a certain range of misalignment.

From Figure 8c, the relationship between M_{12}, M_{34}, and M_{56} can be expressed by

$$\begin{cases} M_{56} = M_{34} \\ M_{34} = aM_{12} + b \end{cases} \tag{13}$$

where a and b are coefficients and the calculated parameters a and b are 0.86 and -6.75×10^{-6}, respectively, when the secondary pads move between 80 mm and 150 mm along the Z-axis transmission distance.

Thus, the total output current of the proposed hybrid topology is rewritten as

$$I_{AB} = \frac{U_{out} M_{12}}{\omega(L_0 L_7 + M_{12}(0.86M_{12} - 6.75 \times 10^{-6}))} + \frac{U_{out}(0.86M_{12} - 6.75 \times 10^{-6})}{\omega L_8 L_9} \tag{14}$$

According to Equation (14), we can obtain the current I_L of the load R_{AB}:

$$I_L = \frac{4}{\pi\sqrt{2}} \frac{U_{out} M_{12}}{\omega(L_0 L_7 + M_{12}(0.86M_{12} - 6.75 \times 10^{-6}))} + \frac{4}{\pi\sqrt{2}} \frac{U_{out}(0.86M_{12} - 6.75 \times 10^{-6})}{\omega L_8 L_9} \tag{15}$$

To simplify the complexity of multi-objective parameter design, inductances L_0 and L_7 are assumed to be equal, and inductance L_8 is also assumed to be equal with inductance L_9. Figure 8 shows that the output current I_L varies with different inductors L_0 and L_8. It can be found that the output current of the series hybrid topology shows a downward concave parabolic trend, while the output current of the LCC-LCC topology shows a monotonous downward trend with the decrease in M_{12}. Therefore, we used the monotonic decreasing characteristic of the LCC-S topology and monotonic increasing characteristic of the LCC-LCC topology to realize the complementary output of the two topologies and ensured the output current was relatively stable. In this article, an acceptable output current fluctuation ratio was limited within 5%, and the rated output current of the load R_{AB} was set to be 6 A. It is clear that the dashed line region in Figure 9 can satisfy the set requirement within an 80–150-mm Z-axis transmission distance. Thus, the values of L_0 and L_7 were both designed to be 15 uH, while L_8 and L_9 were both designed to be 32 uH. Finally, the resonant parameter value of the proposed hybrid topology could be obtained from Equations (1), (3), and (7).

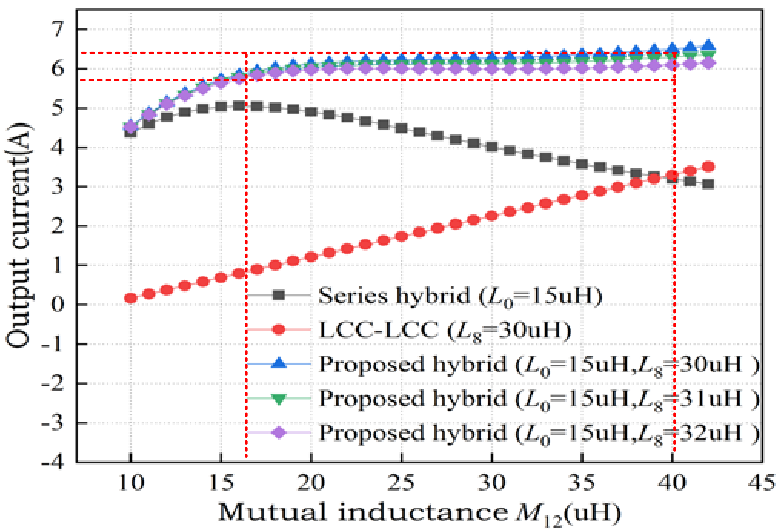

Figure 9. The function of I_L and M_{12} in Z-axis transmission distance.

4. Experimental Verifications

In order to verify the analysis of the proposed method, a 650-W hybrid IPT system was designed and implemented as illustrated Figure 10. The detailed parameters of the system are listed in Table 1. The inverter of the system operated with a fixed frequency and duty cycle control to demonstrate the performance of a constant current output with high misalignment tolerance.

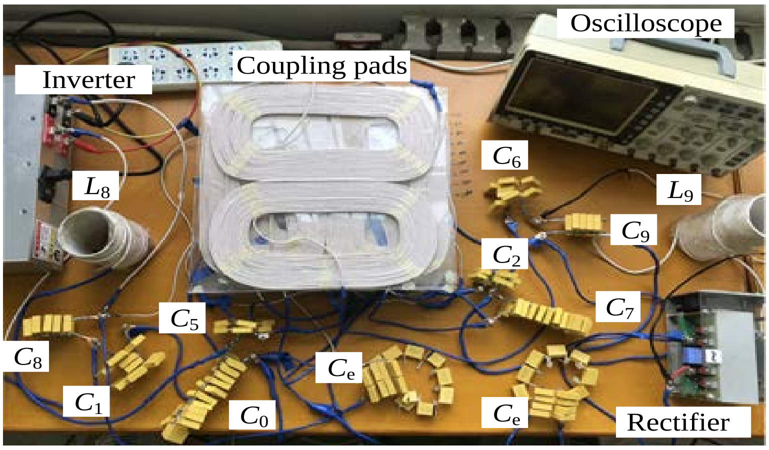

Figure 10. Experimental set-up of the proposed hybrid IPT system.

The output current of the load is drawn in Figure 11, varying with a full load, half load, and quarter load under different Z-axis transmission distances. Within a 80–150-mm Z-axis transmission distance, the output current of the load was between 5.7 A and 6.3 A, which indicates that the output current variation was within 5% when the system worked in the full load and half load conditions. Aside from that, the output current of 4 Ω under the condition of a transmission distance between 110 mm and 130 mm was larger than 6.3 A, which was slightly over the limitation of 5%. Moreover, the output current climbed to the maximum at a 120-mm Z-axis transmission distance. This clearly demonstrates that the proposed hybrid topology with the parameter optimization process had high misalignment tolerance.

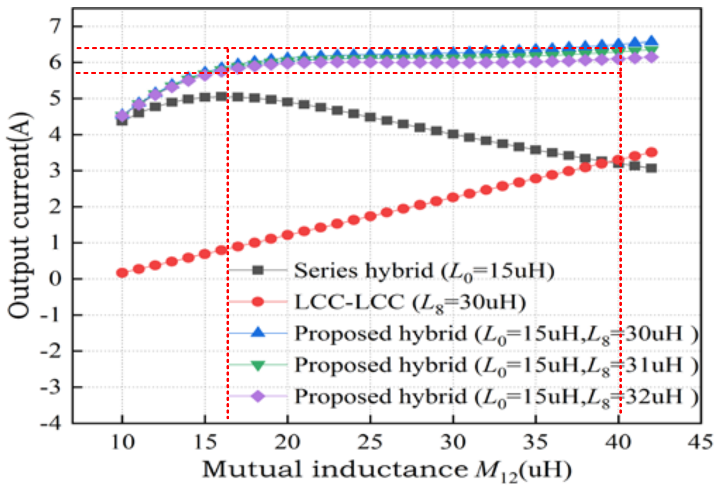

Figure 11. Output current of the proposed hybrid system.

The experimental waveforms of U_{out}, I_{out}, U_L, and I_L with R_L = 17 Ω, 8.5 Ω, and 4 Ω are shown in Figures 12–14 when the Z-axis transmission distance was 80 mm, 120 mm, and 150 mm, respectively. U_{out} and I_{out} are the inverter output voltage and current when the input DC power is 70 V, respectively.

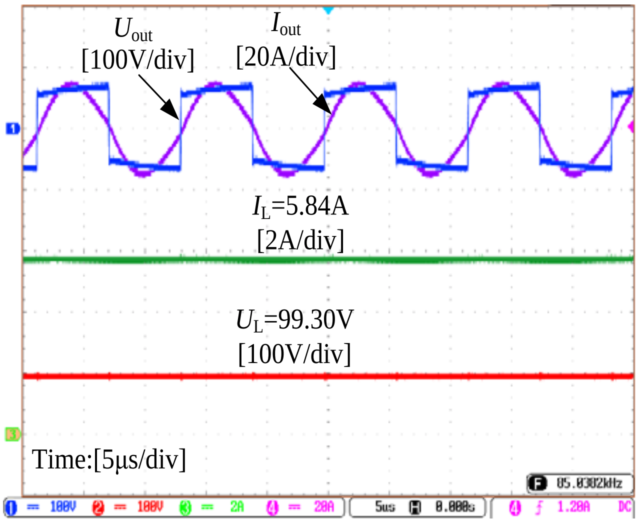

(**a**) the 80-mm *Z*-axis transmission distance

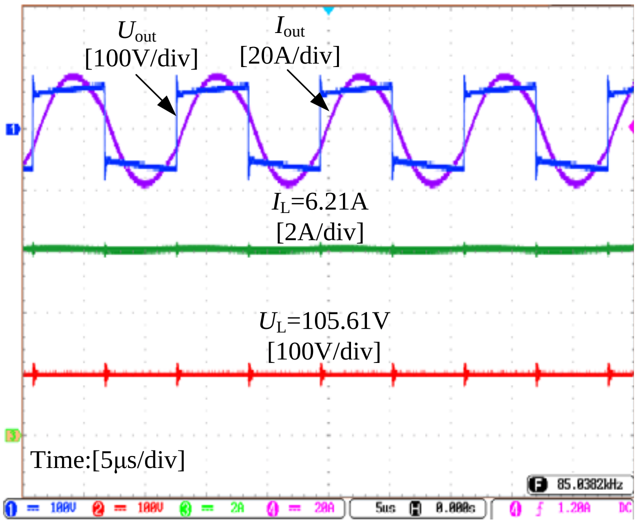

(**b**) the 120-mm *Z*-axis transmission distance

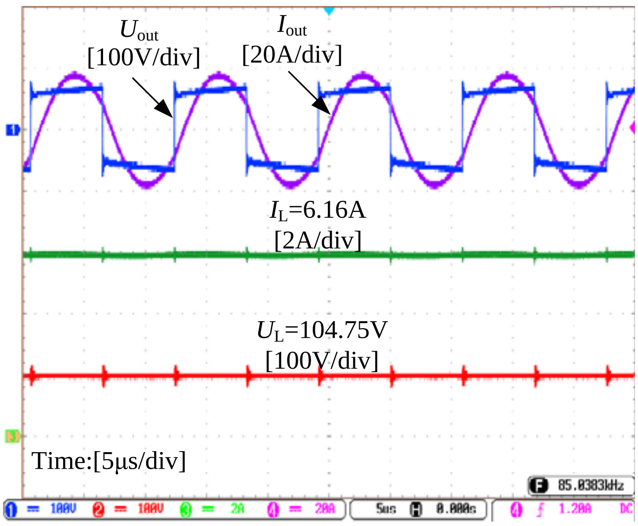

(**c**) the 150-mm *Z*-axis transmission distance

Figure 12. Experimental waveforms of U_{out}, I_{out}, U_L, and I_L for full load with R_L = 17 Ω.

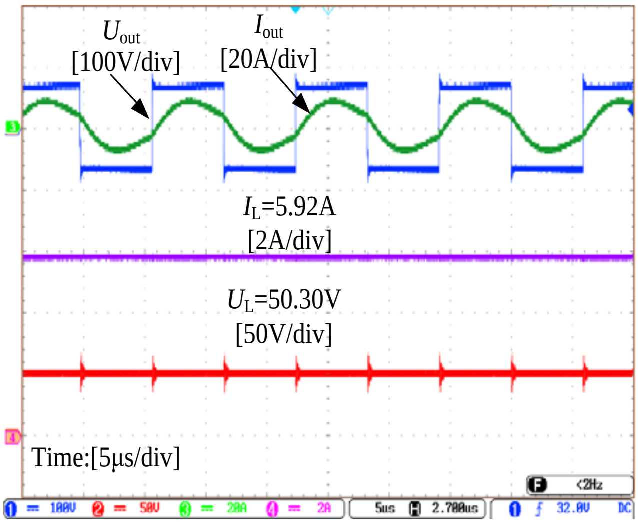

(**a**) the 80-mm *Z*-axis transmission distance

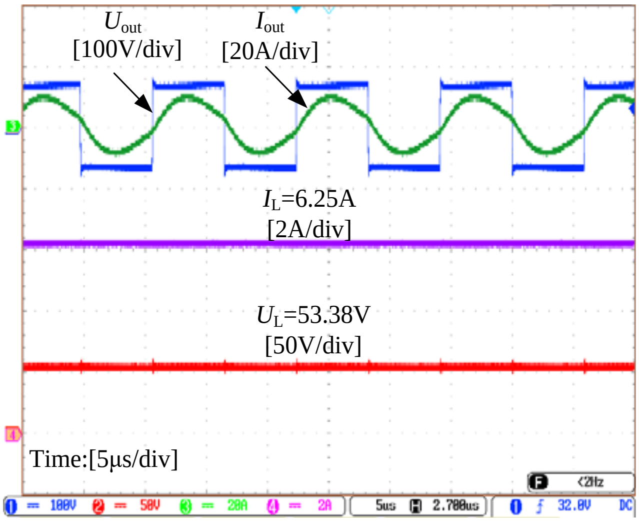

(**b**) the 120-mm *Z*-axis transmission distance

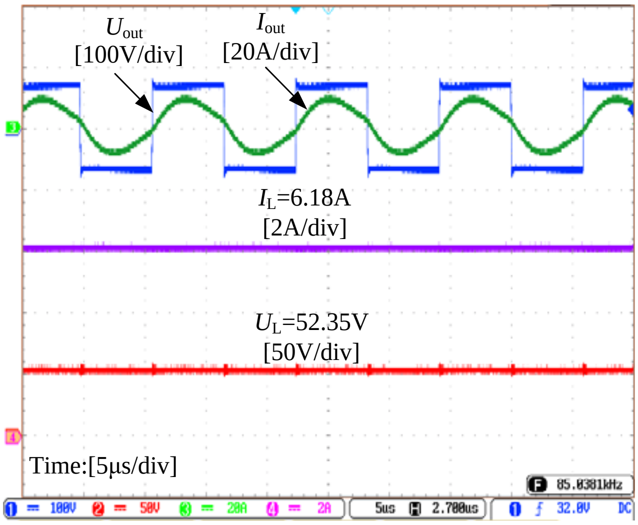

(**c**) the 150-mm *Z*-axis transmission distance

Figure 13. Experimental waveforms of U_{out}, I_{out}, U_L, and I_L for half load with R_L = 8.5 Ω.

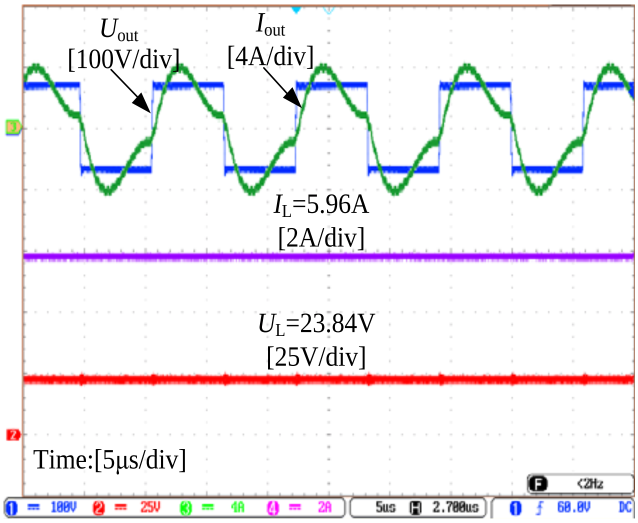

(**a**) the 80-mm *Z*-axis transmission distance

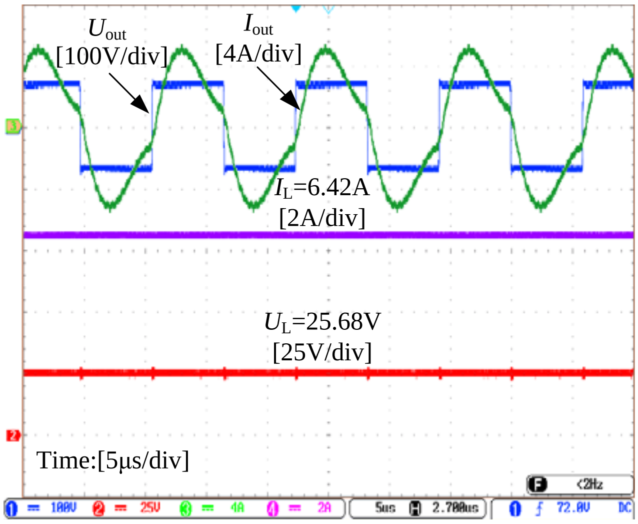

(**b**) the 120-mm *Z*-axis transmission distance

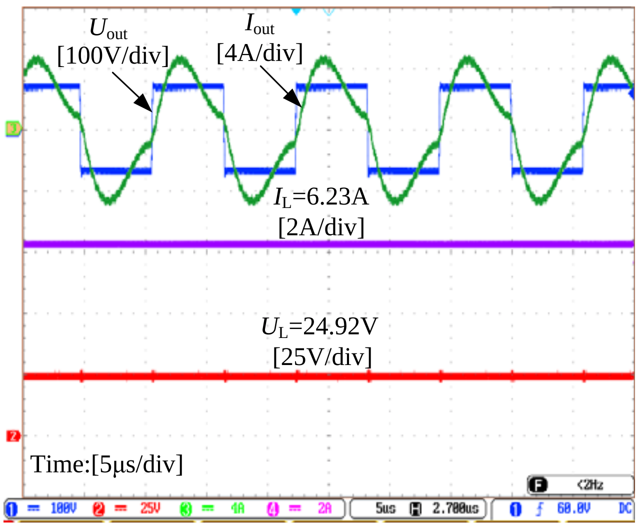

(**c**) the 150-mm *Z*-axis transmission distance

Figure 14. Experimental waveforms of U_{out}, I_{out}, U_L, and I_L for one-quarter load with R_L = 4 Ω.

Figure 12 illustrates the system operating at full load with R_L = 17 Ω. It is clear that ZVS could be achieved between an 80-mm and 150-mm Z-axis transmission distance, which could reduce the switching loss and improve the efficiency. Moreover, the output current was 5.84 A, 6.21 A, and 6.16 A, and the load output voltage was 99.30 V, 105.61 V, and 104.75 V, respectively. Hence, the fluctuation of the load current was within 5% when the variation of the Z-axis transmission distance was within 70%.

Figure 13 shows the system works at half load with R_L = 8.5 Ω. The load output current was 5.92 A, 6.25 A, and 6.18 A, and the load output voltage was 50.30 V, 53.38 V, and 52.35 V, which illustrated the current fluctuation to be 1.33%, 4.17%, and 3.0%, respectively, meeting the design requirements. That aside, the output voltage and current of the inverter were almost in phase, which indicates that soft switching could be achieved and decrease the switching losses.

Figure 14 shows the system operating in a light load conditions when the load was 25% against the fill load with R_L = 4 Ω. The load output current was 5.96 A, 6.42 A, and 6.23 A, and the load output voltage was 23.84 V, 25.68 V, and 24.92 V, which illustrated the current fluctuation to be 0.66%, 7%, and 3.8%, respectively. It is clear that the output current may slightly exceed the limitation of 5% under light load conditions.

Figure 15 clearly illustrates that there is an opposite trend of the output current I_3 of series hybrid topology and the output current I_7 of the LCC-LCC topology when the Z-axis transmission distance varied, and the RMS values of the output currents I_3 and I_7 had a slight deviation from the theoretical analysis in Section 2 due to the influence of parasitic resistance and parameter drift on the resonant parameters. Aside from that, the total output current I_{AB} of the proposed hybrid topology could almost remain stable. Moreover, there was a small phase angle between the output current of the series hybrid topology and LCC-LCC topology because the resonant parameters in the series hybrid topology and LCC-LCC topology operated in a weak inductive state.

Figure 16 shows the output power and efficiency along the Z-axis transmission distance. Figure 16a illustrates that the output power was relatively gentle and consistent with the variation curve of the load output current. The maximum output power was 650 W when the Z-axis transmission distance was 120 mm at full load with R_L = 17 Ω. Figure 16b shows that the efficiency varied with the load and misalignment, and the maximum efficiency could reach 91% with a full load at an 80-mm Z-axis transmission distance.

Some comparisons with traditional control schemes and existing hybrid topologies are listed in Table 2, which are made in terms of control, number of inductors and capacitors, coupling pads, misalignment tolerance, cost, output characteristic, etc. Compared with the traditional control schemes in [9,11], the proposed IPT system can realize a constant current output and misalignment tolerance without additional DC-DC converters and phase shift control, which can simplify the complicated controls. The topologies in [18,21,22] are named the "series hybrid topology", while the topologies in [20] are named the "parallel hybrid topology". These mentioned hybrid topologies all use four coils to transfer power. Aside from that, the number of inductors, capacitors and coupling pads and the cost of the hybrid topologies are higher than the traditional topologies with closed-loop controls. Moreover, the proposed hybrid topology has a wider misalignment tolerance compared with the four-coil hybrid topologies in [18] and [20–22], even though this topology has slightly more components than the other topologies. Thus, the proposed hybrid topology is superior to the traditional control schemes and other hybrid topologies in terms of misalignment tolerance.

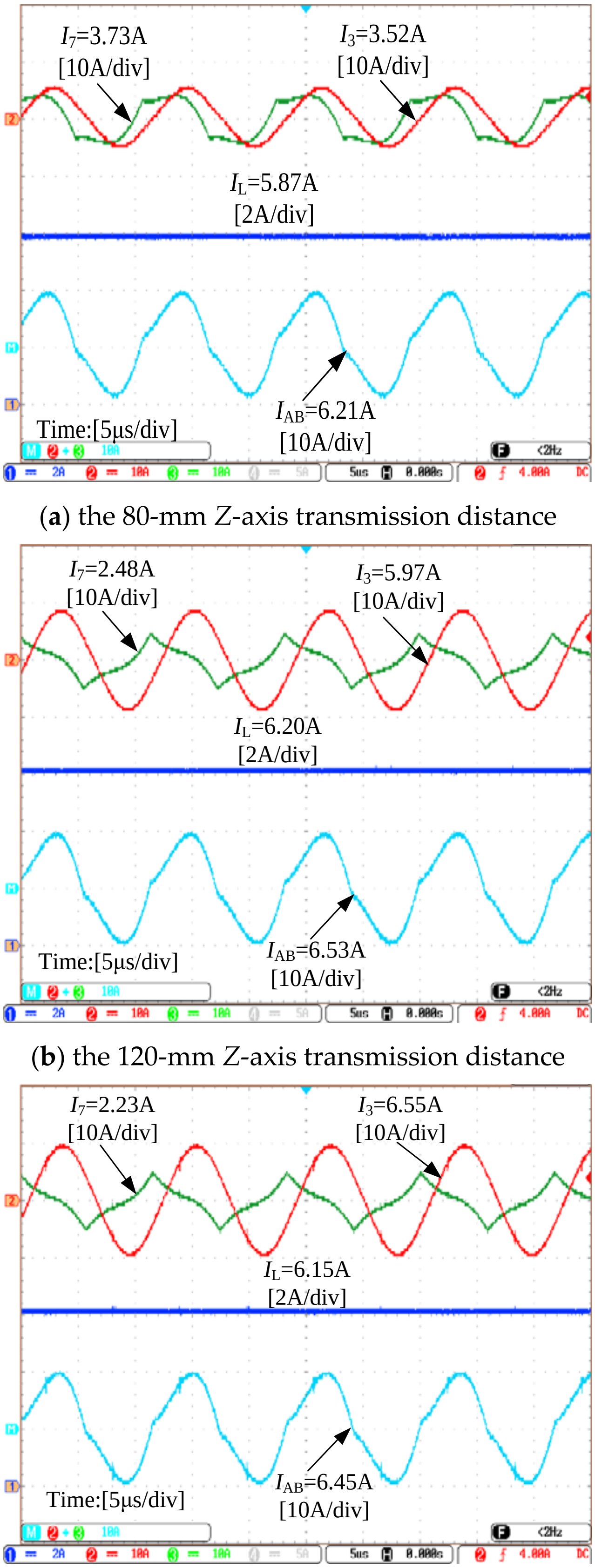

(**a**) the 80-mm *Z*-axis transmission distance

(**b**) the 120-mm *Z*-axis transmission distance

(**c**) the 150-mm *Z*-axis transmission distance

Figure 15. Experimental waveforms of I_3 and I_7 with R_L = 17 Ω.

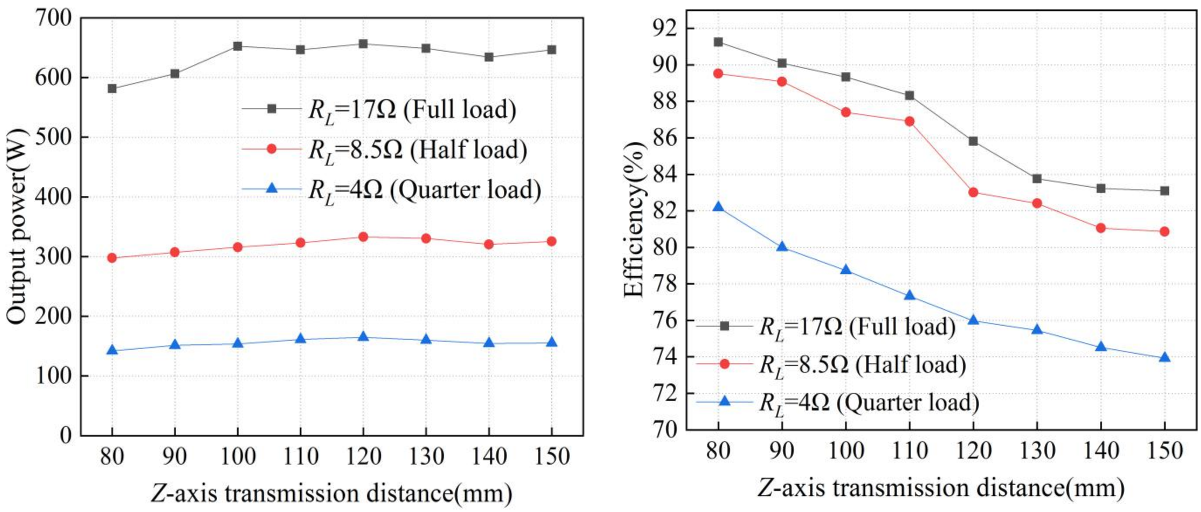

(**a**) output power (**b**) efficiency

Figure 16. Measured output power and efficiency versus transmission distance.

Table 2. Comparison of traditional control schemes and existing hybrid topologies.

	[9]	[11]	[18]	[20]	[21]	[22]	**This Work**
Control	Additional DC-DC	Phase shift control	No	No	No	No	No
Number of inductors	1	0	2	2	0	2	2
Number of capacitors	4	2	6	6	6	6	10
Coupling coils	DD + BP	Q	QDQP	DD	DD	DDQ	DD2Q
Number of coils	3	2	4	4	4	4	6
Cost	High	Low	High	High	High	High	High
Size of coupling pad X * Y * Z (mm)	738 * 391 * 200	360 * 360 * 150	400 * 400 * 150	391 * 738 * 160	775 * 391 * 160	400 * 400 * 150	280 * 280 * 100
Misalignment tolerance (mm)	X:200 (27.5%)	X:140 (38.8%) Z:50 (33.3%)	X:150 (37.5%) Y:150 (37.5%) Z:55(36.6%)	X:160 (40.9%)	Y:160 (40.9%)	X:200 (50%)	Z:70 (70%)
Output characteristic	Constant voltage	Constant voltage	Constant voltage	Constant current	Constant current	Constant voltage	Constant current
Output fluctuation	\	\	5%	\	5%	5%	5%
Peak efficiency	\	90%	93.6%	91%	94%	93%	91%
Wireless communication	No	Yes	No	No	No	No	No

5. Conclusions

A hybrid wireless charging system using DD2Q pads has been presented to improve the misalignment tolerance. The new proposed system, combined with the series hybrid topology and LCC-LCC topology, was studied based on the full mathematical model in the context, where the DD2Q pads consisted of a single-Q coil and orthogonal DD coils. The new pad geometry is able to decouple the cross-mutual inductances so as to realize the independent output of the two topologies. Moreover, a parameter optimization design method on the basis of the characteristics of the DD2Q pads is presented to maintain a stable output current and provide high misalignment tolerance in the *Z*-axis direction. A 650-W hybrid IPT system has been designed and implemented to verify the analysis of the proposed method. The experimental results validate that the proposed hybrid topology can maintain a relatively constant output current at 6 A when the *Z*-axis misalignment varies from −20 to +50 mm, and the output current fluctuation is within 5% when the load varies from 100% full load to 25% light load. In comparison with the conventional hybrid topology, the new proposed system showed a significant improvement in *Z*-axis misalignment tolerance, even though this topology has slightly more components. Moreover, the maximum efficiency can reach 91% when the *Z*-axis transmission distance is 80 mm.

In future research, a thorough economic analysis of the proposed method will be adopted to minimize the system cost, which consists of the number of inductors, capacitors, and coupling coils. That aside, the coupling coil structure should be improved to have better X-, Y-, and Z- misalignment tolerance.

Author Contributions: Conceptualization, Z.G. and J.L.; methodology, Z.G.; software, Z.G. and Y.F.; validation, Z.G., J.L., and X.T.; formal analysis, Z.G.; investigation, Z.G.; resources, Z.G. and J.L.; data curation, Z.G.; writing—original draft preparation, Z.G.; writing—review and editing, Z.G.; visualization, Z.G. and Y.F.; supervision, J.L. and X.T.; project administration, Z.G.; funding acquisition, Z.G. All authors have read and agreed to the published version of the manuscript.

Funding: This research was funded by the Key Research Project of Shaanxi Province of China under Grant 2022GY-310.

Institutional Review Board Statement: Not applicable.

Informed Consent Statement: Not applicable.

Data Availability Statement: Not applicable.

Acknowledgments: This work was supported by the Key Research Project of Shaanxi Province of China under Grants 2021KWZ-20, 2021JY-324, and 2022JQ-424.

Conflicts of Interest: The authors declare no conflict of interest.

References

1. Choi, B.G.; Sohn, Y.-H.; Lee, E.S. Coreless Transmitting Coils with Conductive Magnetic Shield for Wide-Range Ubiquitous IPT. *IEEE Trans. Power Electron.* **2019**, *34*, 2539–2552. [CrossRef]
2. Iruretagoyena, U.; Garcia-Bediaga, A.; Mir, L. Bifurcation Limits and Non-Idealities Effects in a Three-Phase Dynamic IPT System. *IEEE Trans. Power Electron.* **2020**, *35*, 208–219. [CrossRef]
3. Choi, J.S.; Jeong, S.Y.; Choi, B.G. Air-Gap-Insensitive IPT Pad with Ferromagnetic and Conductive Plates. *IEEE Trans. Power Electron.* **2020**, *35*, 7863–7872. [CrossRef]
4. Knecht, O.; Kolar, J.W. Performance Evaluation of Series-Compensated IPT Systems for Transcutaneous Energy Transfer. *IEEE Trans. Power Electron.* **2019**, *34*, 438–451. [CrossRef]
5. Jafari, H.; Olowu, T.O.; Mahmoudi, M. Optimal Design of IPT Bipolar Power Pad for Roadway-Powered EV Charging Systems. *IEEE Can. J. Electr. Comput. Eng.* **2021**, *44*, 350–355. [CrossRef]
6. Kan, T.; Zhang, Y.; Yan, Z. A Rotation-Resilient Wireless Charging System for Lightweight Autonomous Underwater Vehicles. *IEEE Trans. Veh. Technol.* **2018**, *67*, 6935–6942. [CrossRef]
7. Lu, J.; Zhu, G.; Lin, D. Load-Independent Voltage and Current Transfer Characteristics of High-Order Resonant Network in IPT System. *IEEE J. Emerg. Sel. Top. Power Electron.* **2019**, *7*, 422–436. [CrossRef]
8. Dai, X.; Li, X.; Li, Y. Impedance-Matching Range Extension Method for Maximum Power Transfer Tracking in IPT System. *IEEE Trans. Power Electron.* **2018**, *33*, 4419–4428. [CrossRef]
9. Zaheer, A.; Neath, M.; Zhi, H. A Dynamic EV Charging System for Slow Moving Traffic Applications. *IEEE Trans. Power Electron.* **2017**, *3*, 354–368. [CrossRef]
10. Yao, Y.; Wang, Y.; Liu, X. Analysis, Design, and Optimization of LC/S Compensation Topology with Excellent Load-Independent Voltage Output for Inductive Power Transfer. *IEEE Trans. Transp. Electrif.* **2018**, *4*, 767–777. [CrossRef]
11. Yang, L.; Shi, Y.; Wang, M. Constant Voltage Charging and Maximum Efficiency Tracking for WPT Systems Employing Dual-Side Control Scheme. *IEEE J. Emerg. Sel. Top. Power Electron.* **2022**, *10*, 945–955. [CrossRef]
12. Li, Z.; Song, K.; Jiang, J. Constant Current Charging and Maximum Efficiency Tracking Control Scheme for Supercapacitor. *IEEE Trans. Power Electron.* **2022**, *33*, 9088–9100. [CrossRef]
13. Wang, C.; Covic, G.A.; Stielau, O.H. Power Transfer Capability and Bifurcation Phenomena of Loosely Coupled Inductive Power Transfer Systems. *IEEE Trans. Ind. Electron.* **2004**, *51*, 148–157. [CrossRef]
14. Zhang, X.; Liu, F.; Mei, T. Multifrequency Phase-Shifted Control for Multiphase Multiload MCR WPT System to Achieve Targeted Power Distribution and High Misalignment Tolerance. *IEEE Trans. Power Electron.* **2021**, *36*, 991–1003. [CrossRef]
15. Miller, J.; Onar, O.; Chinthavali, M. Primary-Side Power Flow Control of Wireless Power Transfer for Electric Vehicle Charging. *IEEE J. Emerg. Sel. Top. Power Electron.* **2015**, *3*, 147–162. [CrossRef]

16. Chen, Y.; Yang, B.; Zhou, X. A Hybrid Inductive Power Transfer System with Misalignment Tolerance Using Quadruple-D Quadrature Pads. *IEEE Trans. Ind. Electron.* **2020**, *35*, 6039–6049. [CrossRef]
17. Kim, S.; Covic, G.; Boys, J. Tripolar Pad for Inductive Power Transfer Systems for EV Charging. *IEEE Trans. Power Electron.* **2017**, *32*, 5045–5057. [CrossRef]
18. Zhang, Z.; Zhang, B. Angular-Misalignment Insensitive Omnidirectional Wireless Power Transfer. *IEEE Trans. Ind. Electron.* **2020**, *67*, 2755–2764. [CrossRef]
19. Yao, Y.; Wang, Y.; Liu, X.; Pei, Y. A Novel Unsymmetrical Coupling Structure Based on Concentrated Magnetic Flux for High-Misalignment IPT Applications. *IEEE Trans. Power Electron.* **2019**, *34*, 3110–3123. [CrossRef]
20. Zhao, L.; Thrimawithana, D.; Madawala, U. Hybrid Bidirectional Wireless EV Charging System Tolerant to Pad Misalignment. *IEEE Trans. Ind. Electron.* **2017**, *64*, 7079–7086. [CrossRef]
21. Zhao, L.; Thrimawithana, D.J.; Madawala, U.K. A Misalignment-Tolerant Series-Hybrid Wireless EV Charging System with Integrated Magnetics. *IEEE Trans. Power Electron.* **2019**, *34*, 1276–1285. [CrossRef]
22. Qu, X.; Yao, Y.; Wang, D. A Family of Hybrid IPT Topologies with Near Load-Independent Output and High Tolerance to Pad Misalignment. *IEEE Trans. Ind. Electron.* **2020**, *35*, 6867–6877. [CrossRef]